IOP Publishing Mater. Quantum Technol. 5 (2025) 046201 https://doi.org/10.1088/2633-4356/ae09e7

Materials for Quantum Technology

OPEN ACCESS

RECEIVED
13 May 2025

REVISED
16 August 2025

ACCEPTED FOR PUBLICATION
22 September 2025

PUBLISHED
7 October 2025

Original Content from this work may be used under the terms of the Creative Commons Attribution 4.0 licence.

Any further distribution of this work must maintain attribution to the author(s) and the title of the work, journal citation and DOI.

PAPER

Few-mode and anisotropic quantum transport in InSb nanoribbons using an all-van der Waals material-based gate

Colin J Riggert[1], Pim Lueb[2], Tyler Littmann[1], Ghada Badawy[2], Marco Rossi[2], Paul A Crowell[1], Erik P A M Bakkers[2] and Vlad S Pribiag[1,*]

[1] School of Physics and Astronomy, University of Minnesota, Minneapolis, MN 55455, United States of America
[2] Eindhoven University of Technology, Eindhoven, North Brabant 5600, The Netherlands
[*] Author to whom any correspondence should be addressed.

E-mail: vpribiag@umn.edu

Keywords: InSb, quantum transport, *g*-factor anisotropy, few-mode transport, van der Waals gating, nanoribbons

Supplementary material for this article is available online

Abstract

High-quality electrostatic gating is a fundamental ingredient for successful semiconducting device physics, and a key element of realizing clean quantum transport. Inspired by the widespread improvement of transport quality when two-dimensional van der Waals (vdW) materials are gated exclusively by other vdW materials, we have developed a method for gating non-vdW materials with an all-vdW gate stack, consisting of a hexagonal boron nitride dielectric layer and a few-layer graphite gate electrode. We demonstrate this gating approach on MOVPE-grown InSb nanoribbons (NRs), a novel variant of the InSb nanowire, with a flattened cross-section. In our all-vdW gated NR devices we observe conductance features that are reproducible and have low- to near-zero gate hysteresis. We also report quantized conductance, which persists to lower magnetic fields and longer channel lengths than typical InSb nanowire devices reported to date. Additionally, we observe level splitting that is highly anisotropic in an applied magnetic field, which we attribute to the ribbon cross-section. The performance of our devices is consistent with the reduced disorder expected from the all-vdW gating scheme, and marks the first report of ballistic, few-modes quantum transport in a non-vdW material with an all-vdW gate. Our results establish all-vdW gating as a promising approach for high-quality gating of non-vdW materials for quantum transport, which is in principle applicable generically, beyond InSb systems. In addition, the work showcases the specific potential of all-vdW gate/InSb NR devices for enabling clean quantum devices that may be relevant for spintronics and topological superconductivity studies.

1. Introduction

Control of the local electrostatic environment with gating is a cornerstone of semiconducting device physics, essential to reaching the ballistic, phase-coherent, few-mode, and few-electron regimes which define quantum transport [1]. Improving the quality of electrostatic gating is an ongoing effort in the pursuit of ever-cleaner quantum transport. In the study of two-dimensional (2D) van der Waals (vdW) materials, this demand for disorder reduction has led to the development of all-vdW gates [2], which employ hexagonal boron nitride (hBN) as a dielectric layer and few-layer graphite (FLG) as a gate electrode. Thanks to the low charge trap density and absence of dangling bonds of hBN [3–5], the enhanced disorder screening of FLG [6], and the overall atomic flatness of an all-vdW heterostructure, this approach has enabled substantial improvements in the resulting device quality across a range of vdW materials [7–11]. Some effort has been made to expand this technique to the gating of non-vdW materials, with improved transport quality reported in InSb [12, 13] and InAs [14] nanowires when hBN is used with non-vdW gate electrodes, and when FLG is used along with conventional thermal oxide dielectrics [15]. The potential of all-vdW gating of non-vdW materials, however, remains under-explored [16, 17], and the expansion of this technique to the few-modes, quantum transport regime in quasi-one-dimensional (1D) systems has to date remained an open challenge.

© 2025 The Author(s). Published by IOP Publishing Ltd

Here we address this challenge by developing an all-vdW gated semiconductor device platform and employing it to study transport in a novel non-vdW material: an InSb nanoribbon (NR). This NR belongs to the broader class of low-dimensional semiconducting materials with large spin–orbit interaction (SOI) [18], large Landé g-factors [19, 20], and relatively high mobility [21–23], such as InSb and InAs nanowires (NWs), which for more than a decade have underpinned research efforts ranging from topological superconductivity to spin-orbit qubits and spintronics. [24–34]. Compared to NWs, our NRs have a cross section that is wider than it is tall, introducing anisotropy to the transverse quantum confinement. Anisotropic confinement is expected to introduce a magnetic field angle dependence to both the g-factor and subband spacings in high-SOI materials [35–40]. Such angle dependence would enable the decoupling of the semiconductor g-factor from that of other materials, such as the superconductor in a hybrid device. If coexistent with 1D ballistic transport in a NR, this decoupling could offer an additional degree of tunability to topological superconductivity or spintronics devices. However, the quantum transport properties of non-vdW high-SOI NRs have not been studied, and neither ballistic, few-modes transport nor anisotropic field response have been realized. Additionally, high-SOI NR (and NW) devices represent an ideal candidate for exploring the potential of all-vdW gating. This is because they are in most respects an excellent platform for realizing highly-sought physics, such as Majorana zero modes (MZMs)[41–43], yet studies in this field to date have been limited by disorder [44–48], with some of this disorder being potentially introduced by the conventional metal–dielectric gate structures that have been typically used.

Using our all-vdW gated InSb NRs, we report in this work both the first successful realization of ballistic quantum transport in a non-vdW-material with an all-vdW gate, and the first study of the transport properties of non-vdW high-SOI NRs, measured across channel lengths of 1.5 μm, 400 nm, and 200 nm. In all channels, we observe very low to near-zero gate hysteresis, consistent with the reduced charge trap density of the all-vdW gate. In the 200 and 400 nm channels we observe quantized conductance, indicating that the NRs act as ballistic 1D channels [49, 50], and we demonstrate that this quantization survives even in magnetic fields of only a few hundred mT, indicative of low disorder throughout the fabricated NR devices. Finally, we observe field-angle anisotropy of the subband splittings coexistent with 1D ballistic transport, establishing NRs as a promising platform offering enhanced flexibility in experiments which typically use NWs. In the main text of this work, we fully characterize a single NR, with our multi-segment device geometry establishing our three channels as independently-probable segments, testing the NR across a total length of more than 2.5 μm. Full characterization data from an additional, lithographically identical, NR device on a separate all-vdW gate is presented in Supplementary Information section S9, and largely reproduces the results of the main text device.

2. Methods

The NRs used in our devices are grown by metal-organic vapor phase epitaxy alongside symmetric, ultra-thin NWs [15, 22], as shown in figure 1(a). The symmetry-breaking planar expansion of the NRs during growth is likely a consequence of slow, layer-by-layer lateral accumulation occurring alongside the conventional vertical, gold-catalyzed VLS growth, as discussed in [51]. For the NR studied in this work, AFM (figure 1(b)) and SEM scans reveal it to have a width of ∼195 nm, and a height of ∼65 nm, giving a cross sectional aspect ratio of 3:1. A similar cross-sectional aspect ratio is measured for the additional device in the supplemental information. Thus, our NRs can be understood as an intermediate between a sheet-like 2D nanoflake, which occurs when the lateral growth is comparable in rate to the VLS growth [16, 23, 51, 52], and the typical quasi-1D, hexagonally symmetric, NW, which occurs when the axial growth dominates. Importantly, since the NR growth is still VLS-dominated, the NR long axis, and thus transport, lies in the [-111] crystal axis, so that the NR has vanishing Dresselhaus [53] and large Rashba [54] SOC [18].

Our all-vdW gates, schematically illustrated in figure 1(d), were assembled from commercially sourced (hqGraphene) bulk hBN and natural graphite which has been mechanically exfoliated [55] and confirmed by AFM to be clean, atomically flat, and suitably thick (16.7 nm hBN, 0.95 nm FLG for the device in this work). The stack was assembled via a conventional dry transfer technique [56, 57] and deposited onto a substrate prepatterned with Ti/Au (10 nm/90 nm) alignment markers and backgate contact electrodes, such that the electrode touched a corner of the FLG from underneath. The sample was cleaned in hot chloroform to remove polymer residue and vacuum annealed at 400 °C for several hours to further clean the stack surface and remove interfacial bubbles. The NRs were transferred to this gate using a micromanipulator [58], ensuring the NRs sit entirely on the atomically flat portion of the gate, away from the Au electrode. Finally, contacts, patterned by electron beam lithography, were deposited (10 nm/120 nm Ti/Au) after a short *in-situ* Ar ion mill to remove the native oxide at the NR surface. Full fabrication details can be found in Supplementary Information section S1. An optical micrograph of the device studied in this work, along with a characteristic measurement schematic, is presented in figure 1(e). A scanning electron micrograph of the

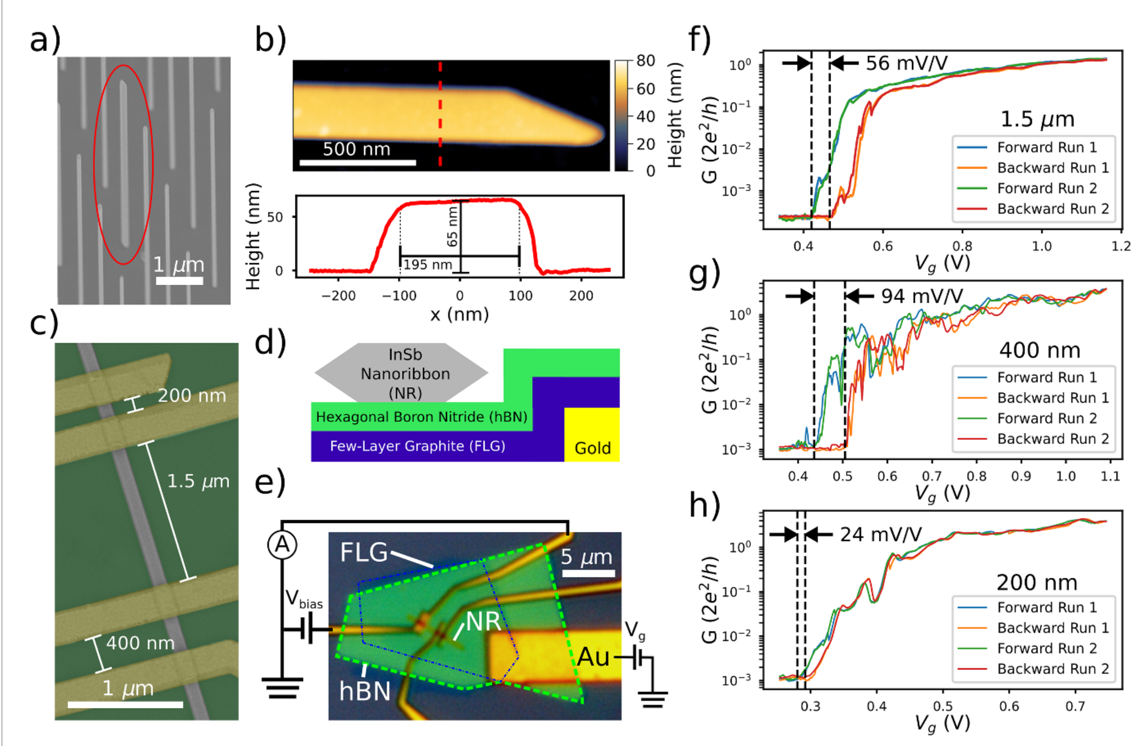

Figure 1. Summary and gate characterization of studied device. (a) Scanning electron micrograph (SEM) of a typical nanowire growth field, with a nanoribbon (NR) circled in red. (b) Atomic force microscope (AFM) scan of the NR used in our device, with a linecut taken at the dashed line. The NR's width is ∼3 times its height. (c) False color SEM image of a lithographically identical device, showing the hBN dielectric (green), Ti/Au contacts (yellow), and NR (grey). Appropriate contact choice allows transport to be studied in uninterrupted channels of nominal length 200 nm, 400 nm, and 1.5 μm. (d) Schematic cross section of the studied device's all-van der Waals-material gate stack, contacted from below by a gold electrode. (e) Optical image of the studied device, with a characteristic DC bias measurement schematically illustrated. (f)–(h) Gate characterization in the 1.5 μm (f), 400 nm (g), and 200 nm (h) channels. Conductance, $G = I_{\text{meas}}/V_{\text{bias}}$, is plotted in for two complete forward and backward loops of the gate voltage, V_g. The difference between forward and backwards threshold voltages is marked, expressed as a ratio with the total gate voltage swept. All channels show low hysteresis and high reproducibility, with the 200 nm channel showing near-zero hysteresis for most values of V_g. V_{bias} is 5 mV in (f), and 1 mV in (g)–(h).

second, lithographically identical device presented in the Supplementary Information is shown in figure 1(c), showing our contact spacing scheme. Measurements were performed in a dilution refrigerator with a base temperature of ∼8 mK using either DC or conventional low-frequency lock-in techniques, as indicated.

3. Experimental results and discussion

3.1. Gate response and hysteresis

To understand the impact of our all-vdW scheme, we first characterize hysteresis and reproducibility in the NR gate response across all channel lengths. For each channel length, the corresponding contacts are DC-biased with V_{bias} (5 mV for the 1.5 μm channel, 1 mV for the 200 and 400 nm channels), and current, I_{meas}, is measured while the gate voltage, V_g, is twice swept forwards and backwards, without resetting to zero between direction changes. The resulting conductance, $G = I_{\text{meas}}/V_{\text{bias}}$, is plotted for each channel in figures 1(f)–(h). To enable comparison across channels, we quantify hysteresis as the ratio of the difference between forward and backward threshold voltages (marked with dashed lines in figures 1(f)–(h) to the total range of gate voltage swept through. We find near-pinchoff hysteresis values of 56 mV/V, 94 mV/V and 24 mV/V for the 1.5 μm, 400 nm, and 200 nm channels, respectively, with the 200 nm hysteresis approaching zero for $V_g \gtrsim 0.35$ V. These values match or outperform hysteresis values in optimized InSb devices on traditional oxide dielectrics [21], including one which we have fabricated and presented in Supplementary Information section S10, and are comparable to values reported in previous InSb devices with hBN dielectrics [13, 16]. This hysteresis behavior was also found to be largely independent of the gate sweep rate, as discussed in Supplementary Information section S2. Additionally, in all channels, we see that the conductance traces, including fluctuations, are reproducible in both sweep directions, indicating that the induced electrostatic environment of our vdW gate and our disorder configuration are stable in time, with minimal temporally-fluctuating charge traps. This combination of low hysteresis and good reproducibility

across multiple channel lengths is consistent with the improved electrostatic gating expected from all our all-vdW approach.

3.2. Quantized conductance in a fixed external magnetic field

To more thoroughly probe the quality of our short (200 nm and 400 nm) channels, we apply an out-of plane magnetic field, $B_z = 2.8$ T, and search for quantized conductance. Because quantized resistance is easily spoiled by even small numbers of scattering events in the confined region, it constitutes a good benchmark of the electronic quality of the completed device and of the potential for using this nanofabrication approach more broadly in experiments requiring few-modes ballistic transport over the inter-contact distance. Using standard lock-in techniques, with an excitation voltage of 50 μV at 19 Hz, we measure differential conductance $G = \mathrm{d}I_{\mathrm{meas}}/\mathrm{d}V_{\mathrm{bias}}$ as function of V_{bias} and V_{g}. The resulting conductance colormaps are shown in figure 2(a) for the 200 nm channel, and figure 2(c) for the 400 nm channel, with linecuts in the V_{g} axis at zero and finite bias shown in figures 2(b) and (d). In both channels, clearly defined plateaus, visible as diamonds of uniform conductance in the colormaps (figures 2(a), (c)) and steps in the linecuts (figures 2(b), (d)) emerge. These plateaus align with half-integer values of the conductance quantum, $G_0 = 2e^2/h$, consistent with Zeeman splitting of the transverse quantum modes. Additionally, in both channels, we observe intermediate-valued plateaus ($G \sim 0.25, 0.75\ G_0$), at finite V_{bias}, a non-linear effect common in clean ballistic 1D systems, which occurs when the source and drain electrode chemical potentials lie in different subbands [59]. Together, this quantized conductance, along with the formation of intermediate plateaus at finite bias convincingly demonstrate that, at this field, our NR hosts ballistic, quasi-1D transport through individual Zeeman-split, spin-resolved subbands [49, 50] at both the 200 and 400 nm length scales.

We note that we have subtracted a finite series resistance, R_{S}, of 12.3 kΩ (13.8 kΩ) from the conductance in the 200 (400) nm channel, which consists of the lump sum of the resistance of our signal line filters (5.7 kΩ), our transimpendance amplifier (3 kΩ), and the total resistance of the interface between the Ti/Au contacts and the NR. Removing the known resistances of the measurement setup, these R_{S} values give total contact resistances of 3.6 and 5.1 kΩ for the 200 and 400 nm channels respectively. In the case of these ballistic channels, R_{S} was determined by subtracting resistance such that the $G = 1.0\ G_0$ plateau in the zero bias linecuts of figures 2(b) and (d) aligned with the quantized value, as is conventionally done in NW devices. However, the multi-probe design of our device allows us to independently determine the series resistance in the 1.5 μm channel as a fitting parameter for the channel's pinchoff curve (see Supplementary Information section S3 for further discussion), where we find $R_{\mathrm{S}} = 12.2$ kΩ, corresponding to a contact resistance of 3.5 kΩ for the 1.5 μm channel. This fitting involves no manual intervention, and so the close agreement in contact resistance with those determined for the ballistic channels, and the fact that contact resistances of a several kΩ are the norm in literature [12, 20, 21, 60, 61], gives us additional confidence in these values.

The quantized plateaus can be used to determine the subband spacings, and thus the g-factor, in both ballistic NR channels. The diamond plateaus in figure 2 close for values of V_{bias} which place the source and drain electrochemical potentials at the bottom of successive subbands, providing a direct measure of the subband splitting in the NR [20]. At $B_z = 2.8$ T, the lowest two subbands in each channel are expected to be the Zeeman-split transverse orbital ground state, so the height of the 0.5 G_0 plateau, $V_{0.5}$, is set by the Zeeman energy, $E_z = |E_{1\downarrow} - E_{1\uparrow}| = |g|\mu_B|\mathbf{B}| = eV_{0.5}$. For the 200 nm channel, we can read off a height of $V_{0.5} \sim 8.2$ mV, corresponding to $|g| \sim 51$. For the 400 nm channel, we can read off $V_{0.5} \sim 9.2$ mV, giving $|g| \sim 57$. Both of these values are reasonably consistent with the g-factor of conventional InSb NW [12, 19, 20, 22, 62, 63], suggesting that InSb NRs are relevant for MZM and spintronic applications where large g-factors are required.

Quantization in quasi-1D InSb NWs with comparable channel lengths to our 400 nm channel is not commonly reported in the literature, with quantization reports typically occurring in channels ∼200 nm in length [12, 20, 22]. Our ballistic transport in the 400 nm channel is therefore indicative of a mean free path at least comparable to the best devices previously reported. Additionally, the 2.8 T external magnetic field we have applied is comparable to or smaller than those typically used to observe quantization in long-channel devices [62]. This magnetic field suppresses backscattering events which destroy quantization in geometrically defined 1D channels such as NWs and NRs [12, 20, 64–66], so the need for a smaller field indicates relatively low disorder in our channel, which is consistent with high quality ballistic transport performance in our all-vdW gated NR device. Further, while quantized conductance in InSb NW devices with channel lengths at or below 200 nm and conventional gating is more widely reported [12, 20, 22, 23, 63], the data from the 200 nm channel of our NR device is exceptionally clean, consistent with the low degree of disorder suggested by the near-zero hysteresis in figure 1(h).

We note that the energy difference between successive Landau levels is ∼23 meV at $B = 2.8$ T, which does not dominate over the energy scale of the subband splitting due to geometric confinement, which we estimate from the plateau heights in figure 2 as ∼10 meV. The relative equal footing of these energy scales at

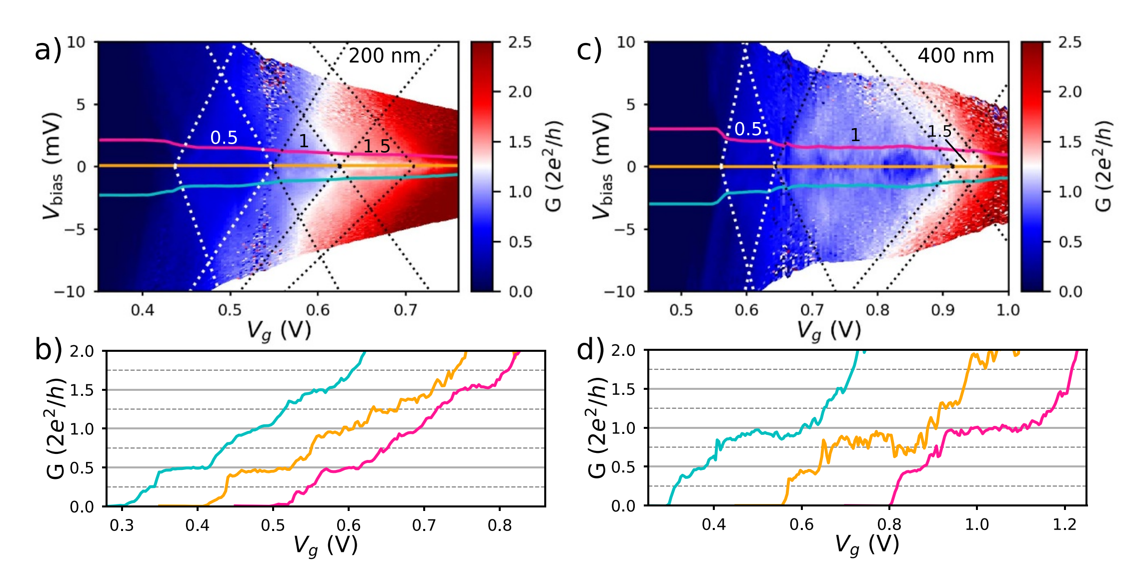

Figure 2. Quantized conductance in a 2.8 T out of plane magnetic field. (a) Differential conductance, $G = dI_{meas}/dV_{bias}$, colormap as a function of V_{bias} and V_g in the 200 nm channel. Diamond-shaped plateaus, marked with dashed lines to guide the eye, are visible at values of 0.5, 1.0 and 1.5 G_0, corresponding to the quantized, ballistic, quasi-1D transport through the first three Zeeman-split subbands in the NR. The dashed lines have been aligned with the plateau edges by following lines of high bias-normalized transconductance, $\partial G/\partial V_g$. (b) Linecuts from (a) at zero (orange) and finite (fuchsia and cyan) biases. For clarity, the positive and negative bias linecuts are offset in V_g by +100 mV and −100 mV respectively. (c) Differential conductance, G, as a function of V_{bias} and V_g in the 400 nm channel. The first three Zeeman-split plateaus are again visible, indicating quantized conductance. (d) Zero and finite bias linecuts from (c), with the positive and negative bias linecuts offset in V_g by +120 mV and −120 mV, respectively. Unannotated versions of panels (a) and (c) are presented in Supplementary Information section S8.

this field indicates that, while orbital effects play a substantial role in determining subband structure [67, 68], the quantized conductance cannot be attributed to the NR hosting a quantum Hall state [69].

3.3. Quantization as a function of external magnetic field strength

To further test the performance of our device, we study the quantization in our 400 nm channel at zero bias as the external out-of-plane magnetic field, B_z, is reduced. The resulting data is plotted in figure 3(a), with dashed lines added to the plateau edges to guide the eye. Linecuts at evenly spaced fields are shown in figure 3(b). Data from the 200 nm channel can be found in the Supplementary Information section S5. In the 400 nm channel, the 0.5 and 1.0 plateau appear to persist and continuously evolve, both in the colormap in figure 3(a) and the linecuts in figure 3(b), through the full range of the field sweep. The width of the 0.5 plateau in V_g monotonically decreases as B_z, and thus E_z, decreases, but only disappears for $B_z = 0$, when the spin degeneracy is restored. The 1.0 G_0 plateau also varies in V_g width, though non-monotonically. As the field is reduced from $B_z = 2.8$ T, it first narrows until $B_z \sim 1$ T, then widens, ultimately persisting at $B_z = 0$. As the 400 nm channel represents the edge of typical mean free path estimates in InSb NW, its quantization serves as a qualitative probe for disorder; the continuous evolution and persistence of plateaus as the backscattering-suppressing field goes to zero thus indicates low disorder in our NR device, potentially a consequence of the vdW gate.

We also note that a resonant feature resembling a residual 0.5 G_0 plateau is present at zero field in figure 3(b), but the higher-field linecuts show that the true 0.5 plateau emerges independent of it. We attribute this resonance to the formation of an incidental quantum dot in the NR at low carrier densities, a common occurrence in 1D transport experiments [70–72]. In our case, the exact origin of this dot is ambiguous, and may involve disorder in the contacts or NR channel, or tunnel barrier formation at the contact interface [36]. This dot resonance also undergoes Zeeman splitting as the field is increased, and we have tracked its evolution with dashed lines in figure 3(a).

Ultimately, we refrain from claiming zero-field quantization, as for low fields, fluctuations in G become more prominent, preserving the plateaus but rendering the quantization increasingly imprecise. This could be due to defects at the NR contact interface introduced by the ion milling of the native oxide prior to contact deposition [31], which act as disorder and cause the contact to act non-Ohmically at low bias for certain values of V_g. The resulting aperiodic suppression of G can be seen prominently in figure 2(c), where several regions of $G < 1.0$ G_0 are visible at low bias throughout the 1.0 plateau, and in figure 2(d), where we observe fluctuations in G at $V_{bias} = 0$ which are greatly reduced at finite bias. The V_g values where these

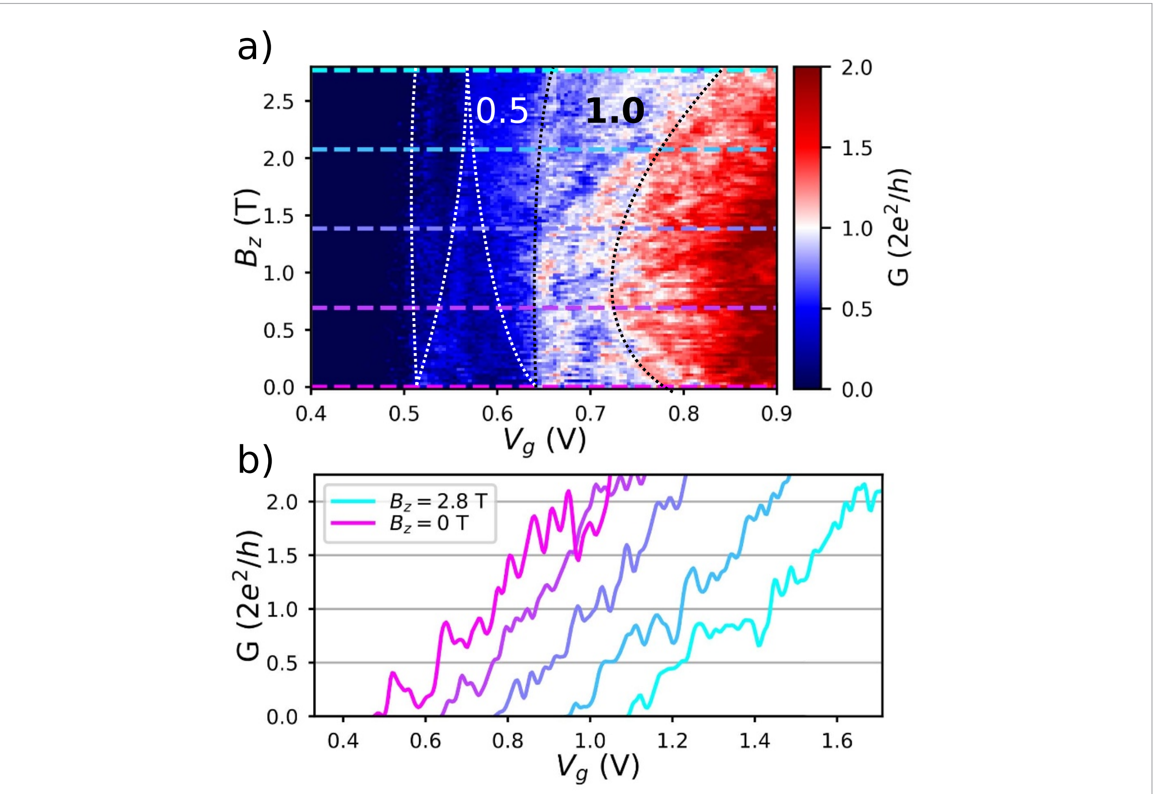

Figure 3. Out-of-plane field sweep, 400 nm channel. (a) Differential conductance at $V_{\mathrm{bias}} = 0$ as a function of V_{g} and out-of-plane magnetic field, B_z. Both the 0.5 and 1.0 G_0 plateaus persist and continuously evolve through the full range of field values. A spin-split resonance is present before the onset of the 0.5 plateau, and is likely a signature of an incidental quantum dot in the NR. Dashed lines mark feature edges as a guide to the eye, and are placed by following lines of high bias-normalized transconductance, $\partial G/\partial V_{\mathrm{g}}$. An unannotated version of this data is presented in Supplementary Information section S8. (b) Linecuts from (a), taken with a uniform spacing of 700 mT, offset in V_{g} by 150 mV, starting from $B_z = 0$.

suppressions occur vary with field, creating 'scars' in the 1.0 plateau in the field scan, as are visible in figure 3(a), which resemble previously reported disorder-induced features [63] that can mimic re-entrant signatures of the helical liquid phase in high-SOI materials [62, 73, 74]. Further discussion of possible contact damage and resistance can be found in Supplementary Information section S4.

3.4. Anisotropic magnetic field response

To probe for anisotropic magnetic field response in our NR, we study the dependence of the quantized conductance on the angle of the applied field. In order to do so, we return to $|\mathbf{B}| = 2.8$ T, and rotate the magnetic field from fully out of the NR plane (i.e. from the z-axis, $\theta = 90°$) to fully in-plane (x-axis, $\theta = 0°$) while applying a fixed $V_{\mathrm{bias}} = 1$ mV across the 400 nm channel. The linear conductance, calculated as $G = I_{\mathrm{meas}}/V_{\mathrm{bias}}$, is plotted in figure 4(b), with linecuts in figure 4(d). Our plateaus persist through all angles of this field sweep, but we observe more pronounced fluctuations in the conductance for angles approaching zero, as seen in the linecuts. This is likely because the NR forms an angle of $\sim$59° with the x-axis, resulting in an increasing portion of the field lying along the NR axis as the field angle is reduced, decreasing the efficacy of back-scattering suppression [65]. Additionally, the suppression of the conductance at low bias becomes more pronounced at low field angles, such that the contiguous 1.0 plateau region has $G < 1.0\ G_0$ for $\theta \lesssim 30°$. Nevertheless, we can still identify anisotropy in the field response. The 0.5 plateau is widest in V_{g} for $\theta \sim 90°$, and subtly narrows with reducing field angle. To quantify this variation, we use the maximum of the bias-normalized transconductance, $\partial G/\partial V_{\mathrm{g}}$, to identify the edges of this plateau, indicated by the white dots superimposed on figure 4(a). Assuming the ratio of the width of the 0.5 plateau in V_{g} to its height in V_{bias} to be angle-independent (see Supplementary Information section S6 for further discussion), we use the previously performed bias spectroscopy at $\theta = 90°$ (figure 2) to convert this measured plateau width into an effective g factor, g_{eff}, as a function of field angle, plotted in figure 4(c). The resulting g_{eff} is largest for field angles near 90°, and is reduced by $\sim$25% as the field angle approaches zero. Anisotropic variation in the V_{g}-width of the 1.0 plateau is much more pronounced, with an approximately threefold reduction in width as the field angle varies from 90° to 0°. Error bars in figures 4(a) and (c) capture the uncertainty in identification of the plateau edges, and thus width, due to the previously mentioned mesoscopic

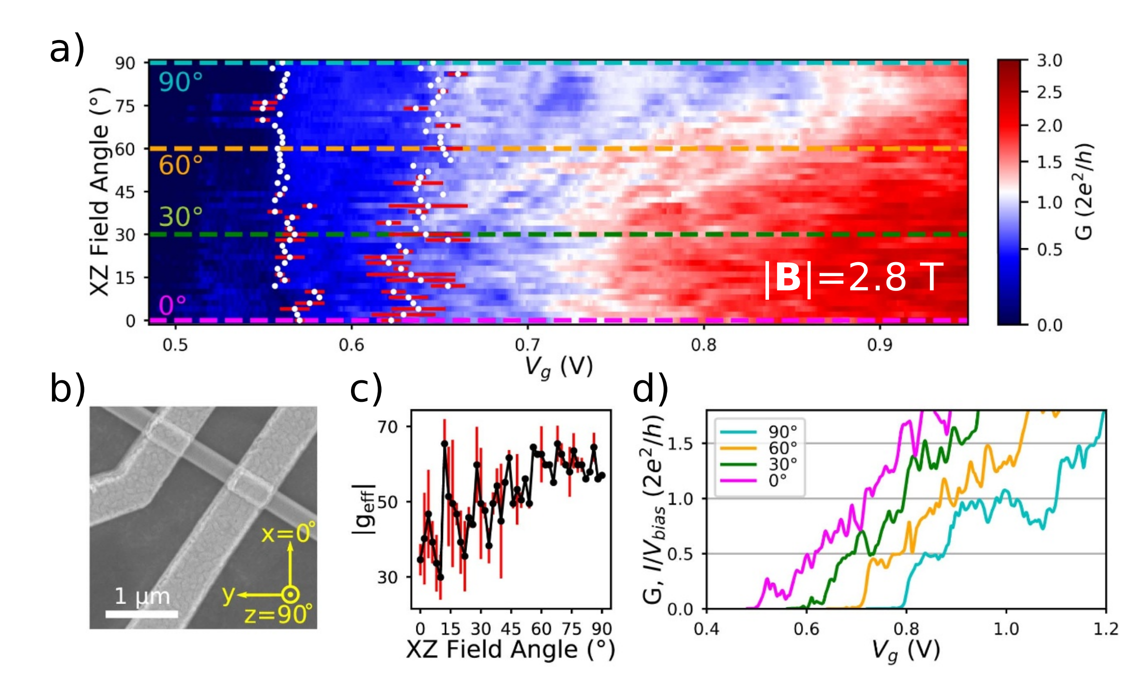

Figure 4. Field rotation from out-of-plane (z-axis, $\theta = 90°$) to in-plane (x-axis, $\theta = 0°$), at $|\mathbf{B}| = 2.8$ T, in the 400 nm channel. (a) Linear conductance, $G = I_{meas}/V_{bias}$, at fixed $V_{bias} = 1$ mV as a function of field angle and V_g. Both the 0.5 and 1.0 plateaus have their width in V_g modulated by the field angle, a consequence of anisotropic confinement from the NR cross-section partially suppressing orbital contributions to both the g-factor and subband spacing as the field angle is reduced from 90°. The edges of the 0.5 plateau are marked with white dots, corresponding to the location of the maximum value of bias-normalized transconductance near the visually identified plateau edge. Error bars capture approximate uncertainty in this edge identification. (b) SEM image of a lithographically identical device showing the coordinate system used for defining field angles. The studied NR lies in the xy-plane and makes an angle of 59° with the x-axis. (c) Effective g factor magnitude, $|g_{eff}|$, as a function of field angle, calculated from the V_g-width of the 0.5 plateau. $|g_{eff}|$ is reduced by ∼25% as the field angle is brought from 90° to 0°. Error bars are propagated from those of (a). (d) Linecuts from (b) at equally spaced field angles, offset in V_g by 80 mV, starting from 0°.

conductance fluctuations. A more detailed discussion of the determination of this uncertainty can be found in Supplementary Information section S7.

To understand the observed anisotropy in both the 0.5 and 1.0 plateaus, we return to the intrinsic anisotropy of the NR. When the field is perpendicular to the NR, the confinement length relevant for field-induced orbital motion—the ∼195 nm NR width—is much larger the electron gyroradius at 2.8T (∼20 nm). This enables the enhancement of the g-factor via SOI, as in bulk InSb, and also causes the subbands to adopt a hybrid magneto-electric character, wherein magneto-orbital effects introduce as an additional effective confining potential, increasing the subband spacing $E_2 - E_1$ in a phenomenon known as magnetic depopulation [37, 49, 67, 68]. As the field is made increasingly parallel to the NR, the relevant confinement length decreases, approaching the NR height, ∼65 nm, as θ approaches 0. This partially suppresses orbital motion in the NR, reducing both the g-factor and the magneto-orbital enhancement of the subband spacing. Such anisotropic field response is common in both quantum dots in gate-defined quantum dots based on InAs [35] and InSb [40] NWs, and in ballistic quantum point contacts (QPCs) on InSb 2D electron gases (2DEGs) [37–39]. In contrast, here the anisotropic response arises naturally from the as-grown quasi-1D confinement, and is not due to gate-induced confinement.

These orbital effects also provide an explanation for the difference in field evolution of the 0.5 and 1.0 G_0 plateaus in figure 3(a). The 0.5 plateau monotonically increases in width with increasing field, as it is a product only of the Zeeman splitting of the spins in the first subband. As the field is increased from zero the width of the 1.0 plateau, which is tied to $E_{2\uparrow} - E_{1\downarrow}$, initially decreases, as Zeeman splitting increases $E_{1\downarrow}$ while decreasing $E_{2\uparrow}$, reducing their separation. However, as the field becomes larger, orbital enhancement of the splitting between the transverse subbands themselves outpaces the Zeeman effect, and $E_{2\uparrow} - E_{1\downarrow}$ begins to instead increase, causing the plateau to widen. This initial narrowing and subsequent broadening of the 1.0 plateau is exactly what we observe in figure 3(a), and further supports the orbital interpretation of anisotropy described above.

4. Conclusion

In conclusion, we have demonstrated a technique for gating non-vdW materials using an all-vdW gate, and have used this gating scheme to perform the first transport characterization of VLS-grown InSb NRs, a novel high-SOI, quantum-confined material. With this platform, we have demonstrated remarkably clean transport in the NRs, including the first realization of few-modes, ballistic quantum transport in a non-vdW material with an all-vdW gate. In particular, we have shown low to near-zero gate hysteresis across length scales of 200 nm, 400 nm, and 1.5 μm, and quantized conductance plateaus in the 200 and 400 nm channels, which qualitatively persists with decreasing external magnetic field to fields as low as a few hundred mT. This behavior is largely reproduced in a lithographically identical second device, detailed in Supplementary Information section S9. These results, and their reproducibility, suggest that the all-vdW gate is effective at reducing disorder when compared to conventional oxide-based gates, and definitively establish NRs as quasi-1D objects, with a mean free path comparable to the best reported InSb NWs. Additionally, we have shown that the Zeeman and subband splittings in the NR studied in this work are anisotropic with the angle of the applied field, owing to the anisotropic transverse confinement and strong SOI in the NR. To our knowledge, such anisotropy is absent from ballistic III-V nanowires.

Our results have several implications. On a broad level, the all-vdW material gate scheme described in this work is a flexible platform. InSb NRs are not uniquely compatible with all-vdW gating, and our bottom–up implementation of vdW gating adds no additional processing steps to the semiconductor itself that a conventional gate approach would not also require. We thus believe our technique can be immediately applied beyond NRs to almost any non-vdW material which can be placed upon a vdW gate stack, and for which extremely high quality, low-hysteresis gating is desired. We also expect that for semiconductors which are compatible with the solvents and annealing temperatures used in depositing and cleaning the vdW gate stack, the stack can be used as a high-quality top gate. The specific case of InSb NRs gated with an all-vdW stack, as we have demonstrated, holds promise as a platform for realizing sought-after phenomena that rely on the ability to fabricate low-disorder gate-tunable ballistic quantum devices in strong-SOI 1D systems. For example, the low-field, long-channel quantized conductance which we have reported is highly conducive to proposed helical liquid experiments [73–75], and with further refinement, the InSb NR/vdW gate platform may aid in definitive observation of the helical liquid state, which would be a major milestone to the conclusive realization of MZMs. Our InSb NR/vdW gate platform is fully compatible with existing techniques, such as sulfur passivation [12, 31] and atomic hydrogen cleaning [76, 77], which have been shown to improve the contact quality of InSb NW devices, and suggest a promising route towards such refinement. Additionally, the g-factor anisotropy in a NR may enable further flexibility in Majorana device design, allowing the decoupling of Zeeman energy from the superconducting gap without introducing the large Dresselahus contributions [37] and possible gate instabilities [39] endemic to existing anisotropic InSb 2DEG QPCs. These benefits are especially relevant to current efforts in selective-area-growth (SAG) methods [78–80], where the full control of aspect ratio allows for the creation of arbitrary NR networks with variable cross-sections, compatible with MZM braiding proposals [81]. Such SAG approaches, as well as recent advances [82] in growing stemless VLS NW networks, which could potentially be adapted for NR growth, represent an avenue toward scalability for the NR geometry.

Data availability statement

The data that support the findings of this study are openly available at the following URL/DOI: https://doi.org/10.5281/zenodo.15 391 898.

Acknowledgments

All aspects of the work at UMN were supported by the Department of Energy under Award No. DE-SC0019274. Nanofabrication work for this Project was conducted in the Minnesota Nano Center (MNC). The cost of MNC user fees for this nanofabrication work was supported by the DOE under award No. DESC0019274. The MNC receives partial support for its operations from the National Science Foundation through the National Nano Coordinated Infrastructure Network (NNCI) under Award Number ECCS-1542202. Eindhoven University of Technology acknowledges the research program ‘Materials for the Quantum Age’ (QuMat) for financial support. This program (registration number 024.005.006) is part of the Gravitation program financed by the Dutch Ministry of Education, Culture and Science (OCW). Eindhoven University of Technology acknowledges European Research Council (ERC TOCINA 834290). We would also like to thank Elliot Bell and Wei Ren for helpful discussions, and Zach Anderson, Chiou Yang Tan, and

Martin Greven at UMN for allowing us to use their vacuum furnace, and providing assistance with the annealing step of device fabrication.

Author contributions

C.J.R. and V.S.P. designed the experiments. C.J.R and T.L. fabricated the devices. C.J.R performed the measurements on all devices and analyzed the data. P.L., G.B., M.R., and E.P.A.M.B. grew the nanoribbons. C.J.R. prepared the manuscript, with input from all authors. V.S.P. and P.A.C. supervised the project.

Conflict of interests

The authors declare no competing interests.

ORCID iDs

Colin J Riggert 0000-0003-1558-067X
Vlad S Pribiag 0000-0003-1784-6347

References

[1] Nazarov Y V and Blanter Y M 2009 *Quantum Transport: Introduction to Nanoscience* (Cambridge University Press)
[2] Rhodes D, Chae S H, Ribeiro-Palau R and Hone J 2019 Disorder in van der Waals heterostructures of 2D materials *Nat. Mater.* **18** 541–9
[3] Dean C R *et al* 2010 Boron nitride substrates for high-quality graphene electronics *Nat. Nanotechnol.* **5** 722–6
[4] Meric I, Dean C, Young A, Hone J, Kim P and Shepard K L 2010 Graphene field-effect transistors based on boron nitride gate dielectrics *Technical Digest - Int. Electron Devices Meeting* (IEDM) pp 4–7
[5] Mayorov A S *et al* 2011 Micrometer-scale ballistic transport in encapsulated graphene at room temperature *Nano Lett.* **11** 2396–9
[6] Ponomarenko L A *et al* 2011 Tunable metal-insulator transition in double-layer graphene heterostructures *Nat. Phys.* **7** 958–61
[7] Hunt B *et al* 2013 Massive Dirac fermions and Hofstadter butterfly in a van der Waals heterostructure *Science* **340** 1427–30
[8] Li L *et al* 2016 Quantum Hall effect in black phosphorus two-dimensional electron system *Nat. Nanotechnol.* **11** 593–7
[9] Zibrov A A, Kometter C, Zhou H, Spanton E, Taniguchi T, Watanabe K, Zaletel M and Young A 2017 Tunable interacting composite fermion phases in a half-filled bilayer-graphene Landau level *Nature* **549** 360–4
[10] Yankowitz M, Chen S, Polshyn H, Zhang Y, Watanabe K, Taniguchi T, Graf D, Young A F and Dean C R 2019 Tuning superconductivity in twisted bilayer graphene *Science* **363** 1059–64
[11] Choi Y *et al* 2019 Electronic correlations in twisted bilayer graphene near the magic angle *Nat. Phys.* **15** 1174–80
[12] Kammhuber J *et al* 2016 Conductance quantization at zero magnetic field in InSb nanowires *Nano Lett.* **16** 3482–6
[13] Jekat F *et al* 2020 Exfoliated hexagonal BN as gate dielectric for InSb nanowire quantum dots with improved gate hysteresis and charge noise *Appl. Phys. Lett.* **116** 253101
[14] Elalaily T *et al* 2021 Gate-controlled supercurrent in epitaxial Al/InAs nanowires *Nano Lett.* **21** 9684–90
[15] Shani L *et al* 2024 Diffusive and ballistic transport in thin InSb nanowire devices using a few-layer-graphene-AlOx gate *Mater. Quantum Technol.* **4** 015101
[16] Zhang L, Chen Y, Pan D, Huang S, Zhao J and Xu H Q 2022 Fabrication and characterization of InSb nanosheet/hBN/graphite heterostructure devices *Nanotechnology* **33** 325303
[17] Liang X, Shamim S, Chen D, Fürst L, Taniguchi T, Watanabe K, Buhmann H, Kleinlein J and Molenkamp L W 2024 Graphite/h-BN van der Waals heterostructure as a gate stack for HgTe quantum wells *Nanotechnology* **35** 345001
[18] van Weperen I, Tarasinski B, Eeltink D, Pribiag V S, Plissard S R, Bakkers E P, Kouwenhoven L P and Wimmer M 2015 Spin-orbit interaction in InSb nanowires *Phys. Rev.* B **91** 1–21
[19] Nilsson H A, Caroff P, Thelander C, Larsson M, Wagner J B, Wernersson L-E, Samuelson L and Xu H Q G 2009 Level-dependent g-factors in InSb nanowire quantum dots *Nano Lett.* **9** 3151–6
[20] van Weperen I, Plissard S R, Bakkers E P A M, Frolov S M and Kouwenhoven L P 2013 Quantized conductance in an InSb nanowire *Nano Lett.* **13** 387–91
[21] Gül O, van Woerkom D J, van Weperen I, Car D, Plissard S R, Bakkers E P A M and Kouwenhoven L P 2015 Towards high mobility InSb nanowire devices *Nanotechnology* **26** 215202
[22] Badawy G, Gazibegovic S, Borsoi F, Heedt S, Wang C-A, Koelling S, Verheijen M A, Kouwenhoven L P and Bakkers E P A M 2019 High mobility stemless InSb nanowires *Nano Lett.* **19** 3575–82
[23] Verma I, Salimian S, Zannier V, Heun S, Rossi F, Ercolani D, Beltram F and Sorba L 2021 High-mobility free-standing InSb nanoflags grown on InP nanowire stems for quantum devices *ACS Appl. Nano Mater.* **4** 5825–33
[24] Nadj-Perge S, Frolov S M, Bakkers E P A M and Kouwenhoven L P 2010 Spin-orbit qubit in a semiconductor nanowire *Nature* **468** 1084–7
[25] Nadj-Perge S, Pribiag V S, van den Berg J W G, Zuo K, Plissard S R, Bakkers E P A M, Frolov S M and Kouwenhoven L P 2012 Spectroscopy of spin-orbit quantum bits in indium antimonide nanowires *Phys. Rev. Lett.* **108** 166801
[26] Mourik V, Zuo K, Frolov S M, Plissard S R, Bakkers E P A M and Kouwenhoven L P 2012 Signatures of Majorana fermions in hybrid superconductor-semiconductor nanowire devices *Science* **336** 1003–7
[27] Pribiag V S, Nadj-Perge S, Frolov S, van den Berg J, van Weperen I, Plissard S, Bakkers E P A M and Kouwenhoven L P 2013 Electrical control of single hole spins in nanowire quantum dots *Nat. Nanotechnol.* **8** 170–4
[28] van den Berg J W G, Nadj-Perge S, Pribiag V S, Plissard S R, Bakkers E P A M, Frolov S M and Kouwenhoven L P 2013 Fast spin-orbit qubit in an indium antimonide nanowire *Phys. Rev. Lett.* **110** 066806
[29] Plissard S R *et al* 2013 Formation and electronic properties of InSb nanocrosses *Nat. Nanotechnol.* **8** 859–64

[30] Szombati D, Nadj-Perge S, Car D, Plissard S, Bakkers E P A M and Kouwenhoven L P 2016 Josephson ϕ_0-junction in nanowire quantum dots *Nat. Phys.* **12** 568–72
[31] Gül O *et al* 2017 Hard superconducting gap in InSb nanowires *Nano Lett.* **17** 2690–6
[32] Gül O *et al* 2018 Ballistic Majorana nanowire devices *Nat. Nanotechnol.* **13** 192–7
[33] Yang Z, Heischmidt B, Gazibegovic S, Badawy G, Car D, Crowell P A, Bakkers E P A M and Pribiag V S 2020 Spin transport in ferromagnet-InSb nanowire quantum devices *Nano Lett.* **20** 3232–9
[34] Dvir T *et al* 2023 Realization of a minimal Kitaev chain in coupled quantum dots *Nature* **614** 445–50
[35] Pryor C E and Flatté M E 2006 Landé g-factors and orbital momentum quenching in semiconductor quantum dots *Phys. Rev. Lett.* **96** 026804
[36] Schwan A, Meiners B-M, Greilich A, Yakovlev D R, Bayer M, Maia A D B, Quivy A A and Henriques A B 2011 Anisotropy of electron and hole g-factors in (In,Ga)As quantum dots *Appl. Phys. Lett.* **99** 221914
[37] Qu F *et al* 2016 Quantized Conductance and large g-factor anisotropy in InSb quantum point contacts *Nano Lett.* **16** 7509–13
[38] Masuda T, Sekine K, Nagase K, Wickramasinghe K S, Mishima T D, Santos M B and Hirayama Y 2018 Transport characteristics of InSb trench-type in-plane gate quantum point contact *Appl. Phys. Lett.* **112** 192103
[39] Lei Z, Lehner C A, Cheah E, Mittag C, Karalic M, Wegscheider W, Ensslin K and Ihn T 2021 Gate-defined quantum point contact in an InSb two-dimensional electron gas *Phys. Rev. Res.* **3** 023042
[40] Mu J, Huang S, Wang J-Y, Huang G-Y, Wang X and Xu H 2020 Measurements of anisotropic g-factors for electrons in InSb nanowire quantum dots *Nanotechnology* **32** 020002
[41] Kitaev A Y 2001 Unpaired Majorana fermions in quantum wires *Phys.-Usp.* **44** 131
[42] Lutchyn R M, Sau J D and Das Sarma S 2010 Majorana fermions and a topological phase transition in semiconductor-superconductor heterostructures *Phys. Rev. Lett.* **105** 077001
[43] Oreg Y, Refael G and von Oppen F 2010 Helical liquids and Majorana bound states in quantum wires *Phys. Rev. Lett.* **105** 177002
[44] Pan H, Liu C X, Wimmer M and Das Sarma S 2021 Quantized and unquantized zero-bias tunneling conductance peaks in Majorana nanowires: conductance below and above $2e^2/h$ *Phys. Rev. B* **103** 214502
[45] Ahn S, Pan H, Woods B, Stanescu T D and Das Sarma S 2021 Estimating disorder and its adverse effects in semiconductor Majorana nanowires *Phys. Rev. Mater.* **124602** 1–35
[46] Frolov S, Zhang P, Zhang B, Jiang Y, Byard S, Mudi S, Chen J, Chen A-H, Hocevar M, Gupta M, Riggert C and Pribiag V S 2023 Smoking gun signatures of topological milestones in trivial materials by measurement fine-tuning and data (arXiv:2309.09368)
[47] Chen J, Woods B, Yu P, Hocevar M, Car D, Plissard S, Bakkers E, Stanescu T and Frolov S 2019 Ubiquitous non-Majorana zero-bias conductance peaks in nanowire devices *Phys. Rev. Lett.* **123** 107703
[48] Das Sarma S and Pan H 2021 Disorder-induced zero-bias peaks in Majorana nanowires *Phys. Rev. B* **103** 1–12
[49] van Wees B J, van Houten H, Beenakker C W J, Williamson J G, Kouwenhoven L P, van der Marel D and Foxon C T 1988 Quantized conductance of point contacts in a two-dimensional electron gas *Phys. Rev. Lett.* **60** 848–50
[50] van Houten H and Beenakker C 1996 Quantum point contacts *Phys. Today* **49** 22–27
[51] Gazibegovic S, Badawy G, Buckers T L J, Leubner P, Shen J, de Vries F K, Koelling S, Kouwenhoven L P, Verheijen M A and Bakkers E P A M 2019 Bottom-up grown 2D InSb nanostructures *Adv. Mater.* **31** 1808181
[52] Rossi M *et al* 2023 Merging nanowires and formation dynamics of bottom–up grown InSb nanoflakes *Adv. Funct. Mater.* **33** 2212029
[53] Dresselhaus G 1955 Spin-orbit coupling effects in Zinc blende structures *Phys. Rev.* **100** 580–6
[54] Rashba E and Sheka V 1959 Symmetry of energy bands in crystals of wurtzite type ii. symmetry of bands with spin-orbit interaction included *Fiz. Tverd. Tela Collect.* **2** 62–76
[55] Huang Y, Sutter E, Shi N N, Zheng J, Yang T, Englund D, Gao H-J and Sutter P 2015 Reliable exfoliation of large-area high-quality flakes of graphene and other two-dimensional materials *ACS Nano* **9** 10612–20
[56] Zomer P J, Guimarães M H D, Brant J C, Tombros N and van Wees B J 2014 Fast pick up technique for high quality heterostructures of bilayer graphene and hexagonal boron nitride *Appl. Phys. Lett.* **105** 013101
[57] Purdie D G, Pugno N, Taniguchi T, Watanabe K, Ferrari A and Lombardo A 2018 Cleaning interfaces in layered materials heterostructures *Nat. Commun.* **9** 5387
[58] Flöhr K *et al* 2011 Manipulating InAs nanowires with submicrometer precision *Rev. Sci. Instrum.* **82** 113705
[59] Kouwenhoven L P, van Wees B J, Harmans C J P M, Williamson J G, van Houten H, Beenakker C W J, Foxon C T and Harris J J 1989 Nonlinear conductance of quantum point contacts *Phys. Rev.* B **39** 8040–3
[60] Fan D, Kang N, Ghalamestani S G, Dick K A and Xu H 2016 Schottky barrier and contact resistance of InSb nanowire field-effect transistors *Nanotechnology* **27** 275204
[61] Plissard S R, Slapak D R, Verheijen M A, Hocevar M, Immink G W G, van Weperen I, Nadj-Perge S, Frolov S M, Kouwenhoven L P and Bakkers E P A M 2012 From InSb nanowires to nanocubes: looking for the sweet spot *Nano Lett.* **12** 1794–8
[62] Kammhuber J *et al* 2017 Conductance through a helical state in an indium antimonide nanowire *Nat. Commun.* **8** 478
[63] Estrada Saldaña J C, Niquet Y-M, Cleuziou J-P, Lee E J H, Car D, Plissard S R, Bakkers E P A M and De Franceschi S 2018 Split-channel ballistic transport in an InSb nanowire *Nano Lett.* **18** 2282–7
[64] van Houten H, Beenakker C W J, van Loosdrecht P H M, Thornton T J, Ahmed H, Pepper M, Foxon C T and Harris J J 1988 Four-terminal magnetoresistance of a two-dimensional electron-gas constriction in the ballistic regime *Phys. Rev. B* **37** 8534–6
[65] Büttiker M 1988 Absence of backscattering in the quantum Hall effect in multiprobe conductors *Phys. Rev. B* **38** 9375–89
[66] van Wees B J, Kouwenhoven L, Willems E, Harmans C, Mooij J, van Houten H, Beenakker C, Williamson J and Foxon C 1991 Quantum ballistic and adiabatic electron transport studied with quantum point contacts *Phys. Rev. B* **43** 12431
[67] Berggren K F, Thornton T, Newson D and Pepper M 1986 Magnetic depopulation of 1D subbands in a narrow 2D electron gas in a GaAs: AlGaAs heterojunction *Phys. Rev. Lett.* **57** 1769
[68] Berggren K-F, Roos G and van Houten H 1988 Characterization of very narrow quasi-one-dimensional quantum channels *Phys. Rev.* B **37** 10118–24
[69] Kouwenhoven L P, Schön G and Sohn L L 1997 *Mesoscopic Electron Transport* (Springer) pp 1–44
[70] Kamimura T and Matsumoto K 2009 Gate induced crossover between Fabry-Pérot and quantum dot behavior in a single walled carbon nanotube hole transistor *J. Appl. Phys.* **106** 113718
[71] Wang L, Pan D, Huang G, Zhao J, Kang N and Xu H 2019 Crossover from Coulomb blockade to ballistic transport in InAs nanowire devices *Nanotechnology* **30** 124001
[72] Gupta M, Khade V, Riggert C, Shani L, Menning G, Lueb P J H, Jung J, Mélin R, Bakkers E P A M and Pribiag V S 2024 Evidence for π-shifted cooper quartets and few-mode transport in pbte nanowire three-terminal Josephson junctions *Nano Lett.* **24** 13903–10

[73] Středa P and Seba P 2003 Antisymmetric spin filtering in one-dimensional electron systems with uniform spin-orbit coupling *Phys. Rev. Lett.* **90** 256601
[74] Pershin Y V, Nesteroff J A and Privman V 2004 Effect of spin-orbit interaction and in-plane magnetic field on the conductance of a quasi-one-dimensional system *Phys. Rev. B* **69** 121306
[75] Rainis D and Loss D 2014 Conductance behavior in nanowires with spin-orbit interaction: a numerical study *Phys. Rev. B* **90** 235415
[76] Webb J L, Knutsson J, Hjort M, Gorji Ghalamestani S, Dick K A, Timm R and Mikkelsen A 2015 Electrical and surface properties of InAs/InSb nanowires cleaned by atomic hydrogen *Nano Lett.* **15** 4865–75
[77] Heedt S *et al* 2021 Shadow-wall lithography of ballistic superconductor–semiconductor quantum devices *Nat. Commun.* **12** 4914
[78] Lee J S *et al* 2019 Selective-area chemical beam epitaxy of in-plane InAs one-dimensional channels grown on InP(001), InP(111)B and InP(011) surfaces *Phys. Rev. Mater.* **3** 084606
[79] Aseev P *et al* 2019 Ballistic InSb nanowires and networks via metal-sown selective area growth *Nano Lett.* **19** 9102–11
[80] Jung J, Schellingerhout S G, Ritter M F, ten Kate S C, van der Molen O A H, de Loijer S, Verheijen M A, Riel H, Nichele F and Bakkers E P A M 2022 Selective area growth of PbTe nanowire networks on InP *Adv. Funct. Mater.* **32** 2208974
[81] Alicea J, Oreg Y, Refael G, Von Oppen F and Fisher M P A 2011 Non-Abelian statistics and topological quantum information processing in 1D wire networks *Nat. Phys.* **7** 412–7
[82] Rossi M, van Schijndel T A J, Lueb P, Badawy G, Jung J, Peeters W H J, Kölling S, Moutanabbir O, Verheijen M A and Bakkers E P A M 2024 Stemless InSb nanowire networks and nanoflakes grown on InP *Nanotechnology* **35** 415602